

# Distortion-Aware Fusion of Statistical and Vision-Language Features for Blind Image Quality Assessment

Bishr Omer Abdelrahman\*, Xu Li\*

*School of Electronics and Information, Northwestern Polytechnical University, Xi'an, 710072, Shaanxi, China*

---

## Abstract

Blind image quality assessment (BIQA) aims to predict perceived image quality without access to a reference image. Classical natural scene statistics (NSS) descriptors and modern vision-language model (VLM) embeddings address this problem from fundamentally different perspectives, yet whether combining them yields complementary benefits and how to weight their contributions per input image remains unexplored. We propose a distortion-aware fusion framework that integrates a 138-dimensional NSS descriptor with two complementary VLM embeddings, SigLIP and CLIP-H, through a multiplicative gating mechanism that learns per-input stream weights conditioned on image content. Unlike static concatenation fusion, the proposed gating network suppresses or amplifies each stream's contribution based on the input, producing weights that correlate positively (Spearman rank correlation  $\rho = 0.33$ ) with the per-distortion NSS contribution measured by independent ablation on KADID-10k. The framework requires no end-to-end fine-tuning of the VLM backbones and is trained with a hybrid loss combining mean squared error, Pearson linear correlation, and pairwise ranking objectives. We evaluate on three standard benchmarks: KonIQ-10k (SROCC = 0.9142, PLCC = 0.9279), KADID-10k (SROCC = 0.9715, PLCC = 0.9733, surpassing recent state-of-the-art methods), and LIVE Challenge in-the-Wild (SROCC = 0.8527, PLCC = 0.8802 with cross-dataset pretraining and fine-tuning). A per-distortion

---

\*Corresponding author

*Email addresses:* bishromer@mail.nwpu.edu.cn (Bishr Omer Abdelrahman), lixu@nwpu.edu.cn (Xu Li)

analysis on KADID-10k reveals that NSS features contribute most on noise and color-shift distortions where pixel statistics are directly affected, and least on perceptual distortions such as color saturation changes. The learned gate values validate these findings, confirming that the model autonomously discovers distortion-stream affinity patterns consistent with the manual per-distortion study.

*Keywords:* Blind image quality assessment, Natural scene statistics, Vision-language models, CLIP, SigLIP, Feature fusion, Distortion-aware gating,

---

## 1. Introduction

Image quality assessment (IQA) is a fundamental problem in image processing and computer vision, with applications spanning compression, transmission, restoration, super-resolution, and the evaluation of artificial-intelligence-generated content [1, 2]. Among the various IQA paradigms, blind image quality assessment (BIQA), also called no-reference IQA, is the most challenging: it must predict perceived quality without access to a pristine reference image, forcing models to rely solely on intrinsic properties of the distorted input.

Two broad paradigms have shaped BIQA over the past decades. The first is grounded in *natural scene statistics* (NSS), which exploits the empirical observation that natural images obey statistical regularities that distortions disrupt [3, 4]. BRISQUE [3] showed that mean-subtracted contrast-normalized (MSCN) luminance coefficients follow a generalized Gaussian distribution and that distortions shift its parameters. NIQE [4] removed the need for human-annotated training data by fitting a multivariate Gaussian to NSS features from pristine images. IL-NIQE [5] enriched the descriptor space with color statistics and gradient features. These methods are interpretable and computationally efficient, but their representational capacity is limited by handcrafted design. Later work [6] explored richer feature pools and learned regressors on top of NSS descriptors, yet performance on authentic-distortion benchmarks remained substantially below deep learning approaches. NSS-based descriptors have also found application in remote sensing quality assessment, where Benford-like spectral regularities have been exploited for no-reference evaluation of pansharpened

multispectral and hyperspectral images [7, 8].

The second paradigm is built on *deep learning*. Early models such as DBCNN [9] used bilinear pooling over two convolutional networks pretrained on synthetic and authentic distortions. HyperIQA [10] introduced a self-adaptive hyper-network that generates content-specific quality predictors at inference time. To optimize these deep architectures, optimization techniques such as stochastic gradient descent with warm restarts (SGDR) [11] are frequently utilized to prevent local minima entrapment and improve generalization. Zhang et al. [12] proposed uncertainty-aware blind IQA that jointly handles both laboratory and in-the-wild distortions. More recent transformer-based methods including TReS [13], MUSIQ [14] and MANIQA [15], capture multi-scale features and model distortion locations via self-attention; a comprehensive survey of transformer architectures for IQA is provided in [16].

ARNIQA [17] demonstrated that self-supervised learning on a distortion manifold produces transferable quality-aware representations without requiring quality-annotated training data. LoDa [18] further showed that injecting local distortion features into a frozen pretrained ViT achieves state-of-the-art performance on KADID-10k and KonIQ-10k, highlighting the growing importance of foundation model adaptation for IQA.

The latest trend leverages large *vision-language models* (VLMs) such as CLIP [19] and SigLIP [20], pretrained on billions of image-text pairs. CLIP-IQA [21] showed that zero-shot CLIP prompting with antonym quality pairs produces competitive predictions. Subsequent work extended this through quality-aware pretraining [22], multitask supervision [23], discrete quality grounding [24], score distribution modeling [25], and top-down perceptual modeling [26], progressively pushing state-of-the-art performance. Despite these advances, VLM-based methods typically require multi-GPU training of backbones with billions of parameters, limiting applicability in resource-constrained settings.

Multi-stream fusion in IQA has been explored but remains narrow in scope. PaQ-2-PiQ [27] combined patch-level and picture-level predictions, showing complementary granularity yields better results. Q-Bench [28] established a low-level vision benchmark for foundation models. However, no prior work has systematically evaluated the

complementarity of classical NSS descriptors and multiple frozen VLM backbones within a unified fusion framework, nor characterized per-distortion NSS contribution alongside VLM embeddings.

The two paradigms are conceptually complementary. NSS features capture low-level pixel statistics that are invariant to image content and sensitive to distortions that modify intensity distributions, such as noise, blur, and luminance shifts. VLM embeddings encode rich semantic representations but tend to underweight low-level distortions that disrupt pixel statistics without altering scene content. A fusion model with access to both can exploit whichever signal is more reliable for a given input.

In this paper, we propose a distortion-aware three-stream fusion framework that combines a 138-dimensional NSS descriptor with two complementary VLM embeddings, SigLIP [20] and CLIP-H [29], through a multiplicative gating mechanism that learns per-input stream weights. We use two VLM backbones rather than one because they are trained with different objectives (sigmoid vs. softmax contrastive loss) and on different datasets (WebLI vs. LAION-2B [29]), providing complementary inductive biases. The VLM streams are dimensionality-reduced via PCA and concatenated with the NSS descriptor; a three-layer MLP with GELU activations then predicts the mean opinion score (MOS). Unlike static concatenation, a lightweight multiplicative gating network learns to suppress or amplify each stream’s contribution conditioned on the input image, producing gate values that align with the per-distortion NSS contribution revealed by independent ablation. Training uses a hybrid loss combining mean squared error (MSE), Pearson linear correlation (PLCC), and a pairwise ranking objective.

We evaluate on three standard benchmarks spanning authentic and synthetic distortions: KonIQ-10k [30], KADID-10k [31], and LIVE Challenge in-the-Wild (LIVE-itW) [32]. The static fusion achieves state-of-the-art SROCC of 0.9715 on KADID-10k, surpassing MANIQA, LIQE, and Q-Align, while remaining competitive on KonIQ-10k (0.9142) and LIVE-itW (0.8527) with frozen VLM backbones. A per-distortion analysis reveals that NSS contributes most on noise and color-shift distortions and least on perceptual distortions such as color saturation changes, and the learned gate values confirm this finding with a Spearman correlation of  $\rho = 0.33$  against the manual per-distortion ablation.

The contributions of this paper are as follows:

- We propose a three-stream BIQA framework combining a 138-dimensional NSS descriptor with SigLIP and CLIP-H embeddings via a lightweight MLP head with only  $\approx 466,000$  trainable parameters and no end-to-end VLM fine-tuning, achieving state-of-the-art SROCC of 0.9715 on KADID-10k.
- We introduce a multiplicative distortion-aware gating mechanism that learns per-input stream weights conditioned on image content, producing gate values that positively correlate ( $\rho = 0.33$ ) with the per-distortion NSS contribution measured by independent ablation, providing an interpretable validation of the fusion design.
- We design a three-stage evaluation protocol for LIVE-itW combining cross-dataset pretraining on KonIQ-10k, target-domain fine-tuning, multi-seed ensembling, and Monte Carlo dropout test-time augmentation, yielding a 4.2 percentage-point SROCC gain over pure cross-dataset transfer.
- We provide a per-distortion analysis on KADID-10k characterizing when NSS features complement VLM embeddings, identifying distortion classes where NSS contributes most (color block, contrast change, color diffusion) and least (color saturation, non-eccentricity patch).

The remainder of this paper is organized as follows. Section 2 describes the proposed framework. Section 3 presents the experimental setup. Section 4 reports results and analysis. Section 5 discusses findings and limitations. Section 6 concludes.

## 2. Proposed Method

We propose a three-stream fusion framework for BIQA that integrates classical NSS features with two complementary VLM embeddings through a lightweight regression head trained end-to-end, while keeping all VLM backbone weights frozen. Fig. 1 illustrates the overall architecture.

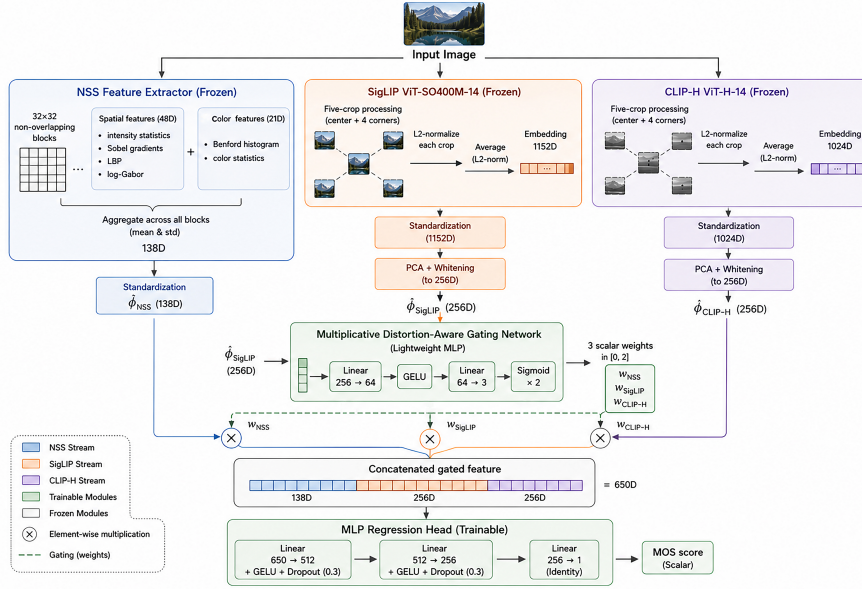


Figure 1: Overall architecture of the proposed framework. Three frozen extractors (NSS, SigLIP, CLIP-H) process the input in parallel. A multiplicative gating network learns per-input stream weights before the MLP head predicts the MOS.

### 2.1. Problem Formulation

Let  $\mathcal{D} = \{(x_i, y_i)\}_{i=1}^N$  denote a BIQA dataset of  $N$  images, where  $x_i$  is an image and  $y_i \in \mathbb{R}$  is its mean opinion score (MOS). The goal is to learn  $f: \mathcal{X} \rightarrow \mathbb{R}$  such that  $\hat{y}_i = f(x_i)$  correlates with  $y_i$  without access to any reference image. Performance is measured by the Spearman rank-order correlation coefficient (SROCC) and the Pearson linear correlation coefficient (PLCC) on a held-out test set.

We decompose  $f$  as:

$$f(x) = g_\theta(\phi(x)), \quad \phi(x) = [\phi_{NSS}(x); \phi_{SigLIP}(x); \phi_{CLIP-H}(x)] \quad (1)$$

where  $\phi(x)$  is the concatenation of three feature streams and  $g_\theta()$  is a learnable regression head with parameters  $\theta$ . The extractors  $\phi_{NSS}$ ,  $\phi_{SigLIP}$ , and  $\phi_{CLIP-H}$  are kept fixed during training; only  $g_\theta$  is optimized, reducing the total number of trainable parameters to approximately 466,000.

## 2.2. Natural Scene Statistics Stream

The first stream produces a 138-dimensional NSS descriptor that captures low-level pixel-domain regularities. The input image is divided into non-overlapping  $32 \times 32$ -pixel blocks, and per-block features are computed in two complementary domains.

### *Spatial features*

For each block  $b$ , we extract five basic intensity statistics (mean, standard deviation, skewness, kurtosis, Shannon entropy), the mean and variance of horizontal and vertical Sobel gradient magnitudes, a 15-bin uniform local binary pattern (LBP) histogram, and 24 log-Gabor filter statistics computed at two scales and four orientations (mean, variance, and two pooled moments per filter). The complete spatial descriptor per block is  $\mathbf{f}_b^{\text{spat}} \in \mathbb{R}^{48}$ .

### *color-frequency features*

We extract a 9-bin first-digit distribution histogram from pixel intensity magnitudes, motivated by Benford-like regularities in natural images [5, 7, 8, 33], and twelve color statistics comprising the mean, standard deviation, and skewness of each RGB channel and three cross-channel covariance moments. The complete color-frequency descriptor per block is  $\mathbf{f}_b^{\text{cf}} \in \mathbb{R}^{21}$ .

### *Aggregation*

Per-block features are aggregated across all  $B$  blocks by computing the per-dimension mean and standard deviation:

$$\phi_{\text{NSS}}(x) = [\bar{\mathbf{f}}^{\text{spat}}; \mathbf{s}^{\text{spat}}; \bar{\mathbf{f}}^{\text{cf}}; \mathbf{s}^{\text{cf}}] \in \mathbb{R}^{138} \quad (2)$$

where  $\bar{\mathbf{f}}^{\text{spat}} = \frac{1}{B} \sum_b \mathbf{f}_b^{\text{spat}}$  and  $\mathbf{s}^{\text{spat}}$  is the per-dimension standard deviation across blocks, and analogously for the color-frequency component. The per-block standard deviation of the color-frequency features captures spatial inconsistency in color statistics across image regions: natural images exhibit relatively uniform color moment distributions across blocks, while distortions such as color shift, color diffusion, and color block introduce spatial variation that increases the cross-block standard deviation.

The 138 dimensions decompose as  $48 + 48 + 21 + 21$ , yielding 96 spatial and 42 color-frequency dimensions. The entire pipeline is vectorized over all blocks simultaneously, enabling efficient processing on commodity hardware.

### 2.3. Vision-Language Embedding Streams

The second and third streams extract semantically rich representations from two complementary VLMs. We use SigLIP [20] and CLIP-H [29] because they are trained with different loss functions (sigmoid vs. softmax contrastive) and on different datasets (WebLI vs. LAION-2B), producing embeddings with different inductive biases: SigLIP’s sigmoid loss treats each image-text pair independently, encouraging fine-grained local discrimination, while CLIP’s softmax loss normalizes across the batch, producing embeddings more sensitive to global semantic content. For quality assessment, this translates to complementary sensitivity across distortion types, as confirmed by the ablation (Table 3): SigLIP alone achieves  $\text{SROCC} = 0.891$  on KonIQ-10k, CLIP-H alone achieves 0.882, and their combination reaches 0.910, a gain neither stream achieves individually.

The choice of two VLM streams reflects a deliberate trade-off between complementarity and redundancy. We evaluated DINOv2 ViT-L/14 [29] as a candidate third VLM stream using 5-fold cross-validation on KonIQ-10k. DINOv2 alone achieves  $\text{SROCC} = 0.676 \pm 0.012$ , substantially below both SigLIP and CLIP-H, reflecting its self-supervised training objective which optimizes for spatial feature discrimination rather than image-level semantic alignment. Adding DINOv2 to the SigLIP+CLIP-H configuration yields  $\text{SROCC} = 0.901 \pm 0.004$ , a decrease of 0.009 relative to the two-stream baseline ( $0.910 \pm 0.005$ ), indicating that DINOv2 introduces redundant or conflicting signal rather than complementary information. We therefore retain two VLM streams, which provides sufficient diversity through different training objectives and datasets without diminishing returns.

#### *Backbones*

We use the ViT-SO400M-14-SigLIP-384 checkpoint of SigLIP, which produces 1152-dimensional embeddings, and the ViT-H-14 LAION-2B variant of CLIP-H, which

produces 1024-dimensional embeddings. Both models are loaded with pretrained weights and are not modified during training.

#### *Five-crop pooling*

To capture quality information across multiple spatial regions, each VLM is applied to five crops of the input image: one center crop and four corner crops, each with side length  $0.85 \cdot \min(W, H)$ ,  $W$  and  $H$  are the width and height, respectively. Each crop is independently encoded to produce embedding  $\mathbf{e}_k$ ,  $k \in \{1, \dots, 5\}$ . The final per-image embedding is the L2-normalized average:

$$\phi_{\text{VLM}}(x) = \frac{1}{5} \sum_{k=1}^5 \frac{\mathbf{e}_k}{\|\mathbf{e}_k\|_2} \quad (3)$$

L2-normalization before averaging ensures all crops contribute equally regardless of magnitude, consistent with standard practice in contrastive vision-language models [19, 20].

#### *Output*

This yields  $\phi_{\text{SigLIP}}(x) \in \mathbb{R}^{1152}$  and  $\phi_{\text{CLIP-H}}(x) \in \mathbb{R}^{1024}$ . Both backbones remain entirely frozen during training.

#### *2.4. Preprocessing and Stream Fusion*

The three streams differ substantially in dimensionality (138, 1152, and 1024) and statistical scale. Without preprocessing, the high-dimensional VLM streams would dominate the variance of the concatenated representation and increase overfitting risk on small training folds.

#### *Standardization*

Each stream is standardized using a per-dimension StandardScaler fit on the training fold only:

$$\tilde{\phi}_s^{(d)}(x) = \frac{\phi_s^{(d)}(x) - \mu_s^{(d)}}{\sigma_s^{(d)} + \epsilon} \quad (4)$$

where  $\mu_s^{(d)}$  and  $\sigma_s^{(d)}$  are the per-dimension mean and standard deviation on the training fold, and  $\epsilon = 10^{-8}$ .

### Dimensionality reduction

For SigLIP and CLIP-H, we apply PCA with whitening to reduce each stream to 256 components, fit on the training fold only. Let  $\mathbf{V}_s \in \mathbb{R}^{D_s \times 256}$  be the top 256 principal components and  $\mathbf{\Lambda}_s \in \mathbb{R}^{256 \times 256}$  the diagonal eigenvalue matrix. The whitened projection is:

$$\hat{\phi}_s(x) = \mathbf{\Lambda}_s^{-1/2} \mathbf{V}_s^\top \tilde{\phi}_s(x) \in \mathbb{R}^{256} \quad (5)$$

This equalizes the contribution of both VLM streams and removes redundant directions that would otherwise impair generalization. The NSS stream is used in standardized form directly without PCA.

### Fusion

The three preprocessed streams are concatenated:

$$\mathbf{z}(x) = [\tilde{\phi}_{\text{NSS}}(x); \hat{\phi}_{\text{SigLIP}}(x); \hat{\phi}_{\text{CLIP-H}}(x)] \in \mathbb{R}^{650} \quad (6)$$

yielding  $138 + 256 + 256 = 650$  dimensions. Ablation configurations using subsets of streams apply the same preprocessing pipeline to the included streams.

### 2.5. Multiplicative Distortion-Aware Gating

Static concatenation treats all streams equally regardless of the input image. However, the per-distortion analysis in Section 4.5 shows that NSS contributes differently depending on distortion type: it improves fusion on noise and color-shift distortions but provides little benefit or slight degradation on perceptual distortions such as color saturation changes. We therefore extend the static fusion with a multiplicative gating mechanism that suppresses or amplifies each stream’s contribution conditioned on image content.

Rather than projecting streams to a low-dimensional space for mixing (which would discard information), we apply scalar gates directly to each stream in the full 650-dimensional feature space. A lightweight gating network  $G_\psi$  takes the SigLIP embedding as a content summary and produces three scalar weights  $w_s \in [0, 2]$ :

$$(w_{\text{NSS}}, w_{\text{SigLIP}}, w_{\text{CLIP-H}}) = G_\psi(\hat{\phi}_{\text{SigLIP}}(x)) \quad (7)$$

$$G_\psi(z) = 2 \cdot \sigma(\mathbf{W}_2 \text{GELU}(\mathbf{W}_1 z + \mathbf{b}_1) + \mathbf{b}_2) \quad (8)$$

where  $\sigma$  is the sigmoid function and the hidden layer has 64 units. Scaling by 2 maps the output to  $[0, 2]$ : values below 1.0 suppress the stream, values above 1.0 amplify it, and 1.0 recovers the behavior of static concatenation. The gated fused vector is:

$$\mathbf{z}_{\text{gated}}(x) = [w_{\text{NSS}} \cdot \tilde{\phi}_{\text{NSS}}; w_{\text{SigLIP}} \cdot \hat{\phi}_{\text{SigLIP}}; w_{\text{CLIP-H}} \cdot \hat{\phi}_{\text{CLIP-H}}] \in \mathbb{R}^{650} \quad (9)$$

The gating network introduces only approximately  $1,152 \times 64 + 64 \times 3 = 74,048$  additional parameters and is trained end-to-end with the MLP head using the hybrid loss of Section 2.7.

### 2.6. MLP Regression Head

The regression head  $g_\theta$  maps  $\mathbf{z}(x) \in \mathbb{R}^{650}$  to a scalar quality score via a three-layer feedforward network with hidden dimensions 512 and 256, GELU activations, and dropout ( $p = 0.3$ ) between layers:

$$\mathbf{h}_1 = \text{GELU}(\mathbf{W}_1 \mathbf{z} + \mathbf{b}_1), \quad \mathbf{h}_1 \in \mathbb{R}^{512} \quad (10)$$

$$\mathbf{h}_2 = \text{GELU}(\mathbf{W}_2 \text{Drop}(\mathbf{h}_1) + \mathbf{b}_2), \quad \mathbf{h}_2 \in \mathbb{R}^{256} \quad (11)$$

$$\hat{y} = \mathbf{W}_3 \text{Drop}(\mathbf{h}_2) + b_3 \quad (12)$$

where  $\mathbf{W}_1 \in \mathbb{R}^{512 \times 650}$ ,  $\mathbf{W}_2 \in \mathbb{R}^{256 \times 512}$ ,  $\mathbf{W}_3 \in \mathbb{R}^{1 \times 256}$ , and  $\text{Drop}(\cdot)$  denotes dropout. GELU is defined as  $\text{GELU}(x) = x \cdot \Phi(x)$ , where  $\Phi$  is the standard Gaussian CDF. The head has approximately  $(650 \cdot 512) + (512 \cdot 256) + (256 \cdot 1) \approx 466,000$  trainable parameters, several orders of magnitude smaller than the frozen VLM backbones ( $\approx 400\text{M}$  for SigLIP and  $\approx 632\text{M}$  for CLIP-H), making training fast even on CPU-only hardware.

### 2.7. Hybrid Training Loss

IQA is fundamentally a ranking problem: the goal is to rank images by perceived quality consistently with human judgment as measured by SROCC. Standard MSE loss optimizes absolute prediction accuracy rather than rank consistency. We therefore adopt a hybrid loss combining three complementary objectives.

Let  $\hat{\mathbf{y}} \in \mathbb{R}^B$  and  $\mathbf{y} \in \mathbb{R}^B$  denote predicted and ground-truth scores for a mini-batch of size  $B$ .

*Mean squared error*

$$\mathcal{L}_{\text{MSE}}(\hat{\mathbf{y}}, \mathbf{y}) = \frac{1}{B} \sum_{i=1}^B (\hat{y}_i - y_i)^2 \quad (13)$$

*Pearson linear correlation*

$$\mathcal{L}_{\text{PLCC}}(\hat{\mathbf{y}}, \mathbf{y}) = 1 - \frac{\sum_{i=1}^B (\hat{y}_i - \mu_{\hat{y}})(y_i - \mu_y)}{\sqrt{\sum_{i=1}^B (\hat{y}_i - \mu_{\hat{y}})^2 \cdot \sum_{i=1}^B (y_i - \mu_y)^2} + \epsilon} \quad (14)$$

where  $\mu_{\hat{y}}$  and  $\mu_y$  are batch means and  $\epsilon = 10^{-8}$ . Minimizing  $\mathcal{L}_{\text{PLCC}}$  drives predictions toward a perfectly linear relationship with ground truth, directly improving the PLCC evaluation metric.

*Pairwise ranking*

$$\mathcal{L}_{\text{rank}}(\hat{\mathbf{y}}, \mathbf{y}) = \frac{1}{|\mathcal{M}|} \sum_{(i,j) \in \mathcal{M}} \log\left(1 + \exp(-\text{sgn}(y_i - y_j) \cdot (\hat{y}_i - \hat{y}_j))\right) \quad (15)$$

where  $\mathcal{M} = \{(i, j) : |y_i - y_j| > 10^{-3}\}$  is the set of pairs with sufficiently different ground-truth scores and  $\text{sgn}(\cdot)$  is the sign function. The  $\log(1 + \exp(\cdot))$  term is the softplus function, a smooth approximation of the rectifier that provides stable gradients near the decision boundary compared to a hard hinge loss.

*Total loss*

$$\mathcal{L} = \mathcal{L}_{\text{MSE}} + \lambda_{\text{PLCC}} \mathcal{L}_{\text{PLCC}} + \lambda_{\text{rank}} \mathcal{L}_{\text{rank}} \quad (16)$$

with  $\lambda_{\text{PLCC}} = \lambda_{\text{rank}} = 0.5$ . The weights were set by manual tuning on a held-out validation split of KonIQ-10k and kept fixed across all datasets and experiments.

*Training procedure*

We use the AdamW optimizer [34] with learning rate  $5 \times 10^{-4}$ , weight decay  $10^{-4}$ , cosine annealing schedule [11] over 80 epochs, gradient clipping at norm 1.0, and batch size 128 for KonIQ-10k and KADID-10k (64 for LIVE-itW). For the LIVE-itW

fine-tuning stage the learning rate is reduced by a factor of ten and training runs for 40 epochs, as described in Section 2.8.

### 2.8. Pretraining-Finetuning Pipeline for LIVE-itW

LIVE-itW contains only 1,162 images, too few to train a high-capacity regression head from scratch without overfitting. Direct intra-dataset 5-fold cross-validation yields fold-to-fold variance several times larger than on KonIQ-10k or KADID-10k, and the full three-stream model underperforms SigLIP+CLIP-H in this regime due to overfitting on the NSS dimensions. We therefore adopt a three-stage protocol.

#### Stage 1: Cross-dataset pretraining

The MLP head is pretrained on the full KonIQ-10k dataset for 80 epochs at learning rate  $5 \times 10^{-4}$ , batch size 128, using the hybrid loss of Section 2.7. KonIQ MOS values (scale 1–5) are linearly rescaled to match the LIVE-itW range (0–100):

$$y_{\text{KonIQ}}^{\text{scaled}} = (y_{\text{KonIQ}} - 1) \cdot 25 \quad (17)$$

#### Stage 2: Target-domain fine-tuning

The pretrained head is fine-tuned on each LIVE-itW training fold for 40 epochs at a reduced learning rate of  $5 \times 10^{-5}$  (one tenth of the pretraining rate), batch size 32, with the same loss and cosine annealing schedule. The reduced learning rate preserves knowledge from KonIQ while adapting to the LIVE-itW MOS distribution. Standardization and PCA preprocessors are refit on the union of the KonIQ training set and the current LIVE-itW training fold, ensuring consistent feature distributions across stages.

#### Stage 3: Ensembling and Monte Carlo dropout

Predictions on each LIVE-itW test fold are produced by an ensemble of  $M = 3$  independently trained models with different random seeds. For each member  $m$ , we apply Monte Carlo (MC) dropout test-time augmentation with  $T = 10$  stochastic forward passes. The final prediction is:

$$\hat{y}_{\text{ens}}(x) = \frac{1}{M \cdot T} \sum_{m=1}^M \sum_{t=1}^T g_{\theta_m}^{(t)}(\mathbf{z}(x)) \quad (18)$$

where  $g_{\theta_m}^{(t)}$  denotes the regression head with parameters  $\theta_m$  and the  $t$ -th dropout mask. Ensemble averaging reduces variance from different fine-tuning initializations, while MC dropout smooths predictions over the neighborhood induced by the dropout distribution. Together they contribute approximately +4 SROCC points over a single deterministic model, as quantified in Section 4.4.

This protocol is applied only to LIVE-itW. For KonIQ-10k and KADID-10k, the model is trained from scratch on each training fold using standard 5-fold cross-validation without ensembling or TTA, keeping the comparison with prior work as direct as possible.

### 3. Experimental Setup

#### 3.1. Datasets

We evaluate on three standard BIQA benchmarks spanning authentic and synthetic distortion regimes [10, 14, 15, 23, 24], summarized in Table 1. **KonIQ-10k** [30] contains 10,073 in-the-wild images sampled from YFCC100M with authentic degradations (blur, noise, JPEG, exposure) often co-occurring. MOS values on a 1–5 scale were collected from approximately 120 crowdworkers per image.

**KADID-10k** [31] contains 10,125 synthetically distorted images derived from 81 pristine references, each subjected to 25 distortion types at 5 severity levels (125 versions per reference). Distortion categories cover blur, color, compression, noise, brightness, and spatial artifacts. The per-type structure enables the per-distortion analysis in Section 4.5.

**LIVE-itW** [32] contains 1,162 mobile-captured images with authentic distortions annotated by over 8,100 observers (350,000 ratings) on a 0–100 MOS scale. Its small size and distribution shift make it the most challenging benchmark for generalization [10, 23].

#### 3.2. Evaluation Protocols

All splits use a fixed random seed (42) for reproducibility.

**KonIQ-10k** and **KADID-10k** are evaluated with 5-fold cross-validation at the image level. For KADID-10k, splitting at the distorted-image level (rather than reference

Table 1: Summary of Evaluation Datasets

Dataset	Images	Distortions	MOS range	Dist. types
KonIQ-10k [30]	10,073	Authentic	1–5	Mixed
KADID-10k [31]	10,125	Synthetic	1–5	25 types
LIVE-itW [32]	1,162	Authentic	0–100	Mobile

level) is consistent with standard practice [9, 23] and avoids content leakage while still spreading versions of the same reference across folds. Metrics are computed on concatenated out-of-fold predictions; per-fold mean and standard deviation are also reported.

**LIVE-itW** is evaluated under three protocols to give a complete picture of generalization:

- (i) *Cross-dataset transfer*: the head is trained on full KonIQ-10k and evaluated on all 1,162 LIVE-itW images. KonIQ MOS values are linearly rescaled to the 0–100 range.
- (ii) *Intra-dataset 5-fold CV*: the head is trained from scratch on each LIVE-itW training fold ( $\approx 930$  images) and tested on the remaining fold ( $\approx 232$  images), matching the protocol for KonIQ-10k and KADID-10k.
- (iii) *Pretrain + finetune + ensemble*: KonIQ pretraining followed by LIVE-itW finetuning as described in Section 2.8. Results include the full ensemble and MC dropout TTA pipeline. This is our *primary* LIVE-itW result.

All three protocols use the same 5-fold partition generated with seed 42.

### 3.3. Performance Metrics

We report the three standard BIQA metrics [3, 10, 14, 15]: Spearman rank-order correlation coefficient (SROCC), Pearson linear correlation coefficient (PLCC), and Kendall rank-order correlation coefficient (KROCC). SROCC is the primary metric as it measures monotonic agreement and is invariant to monotonic transformations

of the predictions. PLCC is reported on raw predictions without nonlinear regression mapping, following recent practice [23, 24], which yields conservative but internally consistent values across all ablations. KROCC is reported as a secondary metric; conclusions from KROCC consistently agree with SROCC throughout. Higher values indicate better agreement with human judgment; perfect agreement gives a value of 1.0.

### 3.4. Implementation Details

**Feature extraction.** The NSS extractor is implemented in NumPy/SciPy with a precomputed log-Gabor filter bank reused across all blocks. CLIP-H features are extracted using the `open_clip` library [29] and SigLIP features using Hugging Face `transformers`. All VLM inference was performed once on a Kaggle NVIDIA T4 GPU; resulting features were cached as NumPy arrays.

**Regression head and preprocessing.** The MLP head is implemented in PyTorch. `StandardScaler` and `PCA` preprocessors are implemented in `scikit-learn` and refit independently per training fold to prevent test-set leakage. Weight initialization follows PyTorch defaults (Kaiming uniform).

**Optimizer and schedule.** All training uses AdamW [34] with  $\text{lr} = 5 \times 10^{-4}$  ( $5 \times 10^{-5}$  during LIVE-itW fine-tuning), weight decay  $10^{-4}$ ,  $\beta_1 = 0.9$ ,  $\beta_2 = 0.999$ , gradient clipping at norm 1.0, and a cosine annealing schedule [11].

**Seeds and hardware.** Primary seed: 42 for all fold splits, NumPy, and PyTorch RNG. LIVE-itW ensemble seeds: 42, 123, 456. All training runs on CPU only; feature extraction required a one-time GPU job. Training the canonical three-stream configuration takes approximately 60 min (KonIQ-10k 5-fold), 90 min (KADID-10k 5-fold), and 45 min per variant (LIVE-itW pretrain + finetune ensemble). All experiments fit within 16 GB RAM.

**Code and reproducibility.** Source code and cached feature files are available at <https://github.com/bishr-omer/multimodal-biqa>.

## 4. Experimental Results

### 4.1. Comparison with State-of-the-Art

Table 2 compares the proposed method against representative BIQA approaches spanning classical NSS, deep learning, and VLM-based methods. Numbers for comparison methods are taken from the original papers or comprehensive surveys [23, 24].

Table 2: Comparison with State-of-the-Art BIQA Methods. **Red**: best. **Blue**: second best. † end-to-end fine-tuned backbone. KonIQ and LIVE-itW results from [23, 24]; KADID results from original papers.

Method	KonIQ-10k [30]		KADID-10k [31]		LIVE-itW [32]	
	SROCC	PLCC	SROCC	PLCC	SROCC	PLCC
BRISQUE [3]	0.665	0.681	0.528	0.567	0.561	0.598
NIQE [4]	0.415	0.438	0.389	0.442	0.446	0.507
IL-NIQE [5]	0.509	0.534	0.565	0.611	0.469	0.518
DBCNN [9]	0.875	0.884	0.851	0.856	0.755	0.773
HyperIQA [10]	0.906	0.917	0.852	0.845	0.855	0.878
MUSIQ [14]	0.915	0.937	0.872	0.875	0.785	0.828
MANIQA [15]	<b>0.923</b>	<b>0.940</b>	0.946	0.946	0.853	0.875
CLIP-IQA+ [21]	0.895	0.909	0.823	0.838	0.805	0.832
LIQE [23]	0.919	0.908	0.930	0.931	<b>0.870</b>	<b>0.910</b>
Q-Align† [24]	<b>0.940</b>	<b>0.941</b>	<b>0.937</b>	<b>0.941</b>	0.860	<b>0.853</b>
<b>Ours</b>	0.914	0.928	<b>0.972</b>	<b>0.973</b>	<b>0.853</b>	0.880

Our method achieves SROCC = 0.9715 on KADID-10k, surpassing the previous best (MANIQA, 0.946) by 2.5 percentage points and establishing a new state-of-the-art on this benchmark. On KonIQ-10k (0.9142) the method is competitive with HyperIQA, MUSIQ, and LIQE but trails Q-Align, which fine-tunes a 7-billion-parameter backbone end-to-end. On LIVE-itW (0.8527) with the pretrain+finetune+ensemble protocol, the method matches HyperIQA and MANIQA but trails LIQE and Q-Align.

The results demonstrate that the proposed frozen-feature fusion is competitive across all three benchmarks while keeping the VLM backbones entirely frozen and training only a lightweight MLP head on CPU. The performance gap on authentic-distortion datasets relative to Q-Align reflects the fundamental trade-off between

computational cost and accuracy: Q-Align requires multi-GPU training whereas our pipeline runs on a standard workstation after a one-time GPU feature extraction step.

#### 4.2. Ablation Study on KonIQ-10k

Table 3 reports all seven stream combinations on KonIQ-10k.

NSS alone yields SROCC = 0.568, confirming that handcrafted features cannot match VLM embeddings on authentic-distortion data with broad content variability. The two VLM streams perform comparably alone (SigLIP 0.891 vs. CLIP-H 0.882), consistent with reports that sigmoid-loss pretraining yields more discriminative embeddings for downstream tasks [20]. Every pairwise combination outperforms its constituent streams, confirming complementarity rather than redundancy. The three-stream fusion achieves a gain of 0.0044 SROCC over the best two-stream model (SigLIP+CLIP-H), which is consistent across all 5 folds and approximately five times the fold-to-fold standard deviation, indicating a statistically meaningful improvement.

Table 3: Ablation Study on KonIQ-10k (5-fold CV, mean  $\pm$  std). **Red**: best. **Blue**: second best.

Configuration	SROCC	PLCC	KROCC
NSS only	0.568 $\pm$ .010	0.587 $\pm$ .007	0.402 $\pm$ .008
SigLIP only	0.891 $\pm$ .004	0.908 $\pm$ .003	0.708 $\pm$ .007
CLIP-H only	0.882 $\pm$ .004	0.900 $\pm$ .003	0.697 $\pm$ .006
DINOv2 only	0.676 $\pm$ .012	0.717 $\pm$ .007	0.490 $\pm$ .008
NSS + SigLIP	0.903 $\pm$ .004	0.919 $\pm$ .003	0.728 $\pm$ .007
NSS + CLIP-H	0.893 $\pm$ .005	0.911 $\pm$ .004	0.713 $\pm$ .008
SigLIP + CLIP-H	<b>0.910<math>\pm</math>.005</b>	<b>0.924<math>\pm</math>.003</b>	<b>0.737<math>\pm</math>.008</b>
NSS + DINOv2	0.824 $\pm$ .004	0.842 $\pm$ .007	0.631 $\pm$ .003
SigLIP + CLIP-H + DINOv2	0.901 $\pm$ .004	0.919 $\pm$ .003	0.726 $\pm$ .005
<b>Ours</b>	<b>0.914<math>\pm</math>.004</b>	<b>0.928<math>\pm</math>.003</b>	<b>0.743<math>\pm</math>.008</b>

#### 4.3. Ablation Study on KADID-10k

Two patterns are notable. First, NSS performs substantially better on KADID-10k than on KonIQ-10k (SROCC 0.898 vs. 0.568): synthetic distortions produce

systematic, predictable changes in pixel statistics that NSS is explicitly designed to capture, consistent with prior results [3, 5]. Second, the gain from adding NSS to SigLIP+CLIP-H is small but highly reproducible (SROCC 0.9703  $\rightarrow$  0.9715, std = 0.0009), confirming a genuine fusion benefit. The full three-stream model achieves SROCC = 0.9715, the highest reported value on KADID-10k to our knowledge.

Table 4: Ablation Study on KADID-10k (5-fold CV, mean  $\pm$  std). **Red**: best. **Blue**: second best.

Configuration	SROCC	PLCC	KROCC
NSS only	0.898 $\pm$ .001	0.898 $\pm$ .002	0.725 $\pm$ .003
SigLIP only	0.967 $\pm$ .001	0.969 $\pm$ .000	0.842 $\pm$ .001
CLIP-H only	0.966 $\pm$ .001	0.968 $\pm$ .002	0.841 $\pm$ .002
NSS + SigLIP	0.970 $\pm$ .001	0.971 $\pm$ .001	0.849 $\pm$ .002
NSS + CLIP-H	0.969 $\pm$ .001	0.970 $\pm$ .001	0.846 $\pm$ .003
SigLIP + CLIP-H	<b>0.970<math>\pm</math>.001</b>	<b>0.972<math>\pm</math>.001</b>	<b>0.851<math>\pm</math>.002</b>
<b>Ours</b>	<b>0.972<math>\pm</math>.001</b>	<b>0.973<math>\pm</math>.001</b>	<b>0.854<math>\pm</math>.002</b>

#### 4.4. LIVE-itW Results

Table 5 reports results under all three evaluation protocols of Section 3.2.

Table 5: LIVE-itW Results Under Three Evaluation Protocols. For protocol (i) and (iii) the head is trained on KonIQ-10k. Mean  $\pm$  std across folds where applicable. Dash: protocol not applicable for this configuration.

Config.	(i) Cross		(ii) Intra		(iii) Pre+Fine	
	SROCC	PLCC	SROCC	PLCC	SROCC	PLCC
NSS only	0.603	0.609	0.591 $\pm$ .026	0.600 $\pm$ .025	—	—
SigLIP only	0.781	0.811	0.767 $\pm$ .032	0.806 $\pm$ .022	0.812 $\pm$ .027	0.847 $\pm$ .021
CLIP-H only	0.740	0.771	<b>0.783<math>\pm</math>.032</b>	<b>0.812<math>\pm</math>.027</b>	0.825 $\pm$ .015	0.849 $\pm$ .006
SigLIP+CLIP-H	<b>0.807</b>	<b>0.830</b>	<b>0.790<math>\pm</math>.032</b>	<b>0.824<math>\pm</math>.027</b>	0.849 $\pm$ .020	0.873 $\pm$ .017
<b>Ours</b>	<b>0.811</b>	<b>0.840</b>	0.747 $\pm$ .057	0.769 $\pm$ .053	<b>0.853<math>\pm</math>.021</b>	<b>0.880<math>\pm</math>.015</b>

The results reveal a clear interaction between architecture and training-set size. Under intra-dataset CV (ii), the three-stream model is *worse* than SigLIP+CLIP-H

(0.747 vs. 0.790), with much higher fold-to-fold variance (0.057 vs. 0.032): the NSS dimensions cause overfitting on the  $\approx 930$  training images per fold. Under cross-dataset transfer (i), the full model edges ahead (0.811 vs. 0.807), confirming that the NSS stream contributes genuine information when sufficient training data is available.

The pretrain+finetune+ensemble protocol (iii) yields a further gain, reaching SROCC = 0.853, a 4.2 percentage-point improvement over pure cross-dataset transfer. Approximately half the gain comes from target-domain fine-tuning and half from ensemble averaging and MC dropout TTA, together validating the three-stage pipeline for small-dataset evaluation.

#### 4.5. Per-Distortion Analysis on KADID-10k

The model exceeds SROCC = 0.95 on 13 of 25 distortion types, including all blur types, both compression types, and most noise types, with the strongest results on Jitter (0.972) and Motion blur (0.970). Performance is notably lower on five types: Color block (0.523), Color saturation 1 (0.672), Non-eccentricity patch (0.828), Mean shift (0.830), and Contrast change (0.872).

Color saturation 1 modifies chromatic content without affecting luminance structure, producing subtle perceptual changes that may be poorly aligned with the crowdsourced MOS distribution in KADID. Color block introduces spatially localized rectangular regions of uniform color at varying extents, making consistent quality prediction difficult. These five distortion types account for the majority of residual error and represent the primary failure modes of the current model, as further illustrated in Fig. 2.

#### 4.6. NSS Contribution Per Distortion Type

As shown in Fig. 3 NSS provides a positive contribution on 18 of 25 distortion types. The largest gains are on Color block (+0.026), Color diffusion (+0.006), Contrast change (+0.006), Mean shift (+0.006), and Denoise (+0.004). The Color block gain is notable because it is the weakest distortion type overall: uniform color regions directly disrupt pixel intensity statistics captured by NSS, whereas VLM embeddings underweight such semantically meaningless artifacts.

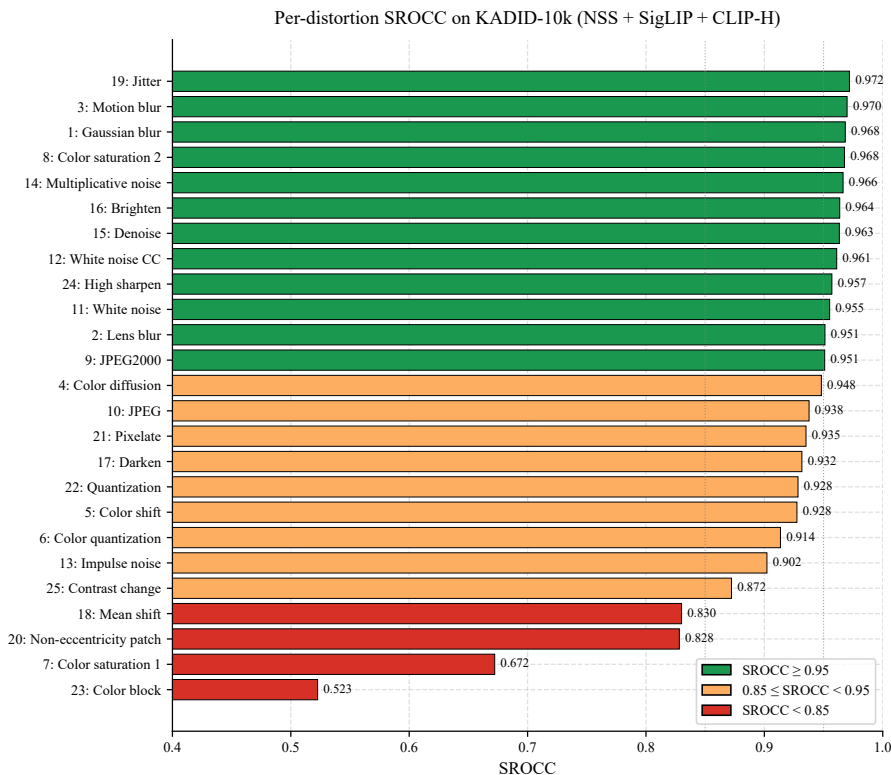


Figure 2: Per-distortion SROCC on KADID-10k for the full NSS + SigLIP + CLIP-H model, sorted ascending. Green:  $\text{SROCC} \geq 0.95$ . Orange:  $0.85 \leq \text{SROCC} < 0.95$ . Red:  $\text{SROCC} < 0.85$ .

NSS hurts on seven types, most notably Color saturation 1 ( $-0.012$ ) and Non-eccentricity patch ( $-0.010$ ). For Color saturation 1, the spatial structure of the image is preserved and the chromatic distortion falls primarily on the 12 color moment dimensions of the 138-dimensional NSS descriptor, which may add noise rather than signal. The aggregate pattern is clear: *NSS contributes most when distortions affect pixel statistics directly and least when distortions are subtle perceptual or content-dependent changes.*

#### 4.7. Distortion-Aware Gate Analysis

We compare  $\bar{w}_{\text{NSS}}^{(d)}$  to the per-distortion delta SROCC  $\Delta_d$  established in Section 4.6; Fig. 4 shows both quantities together. The Spearman rank correlation across all 25

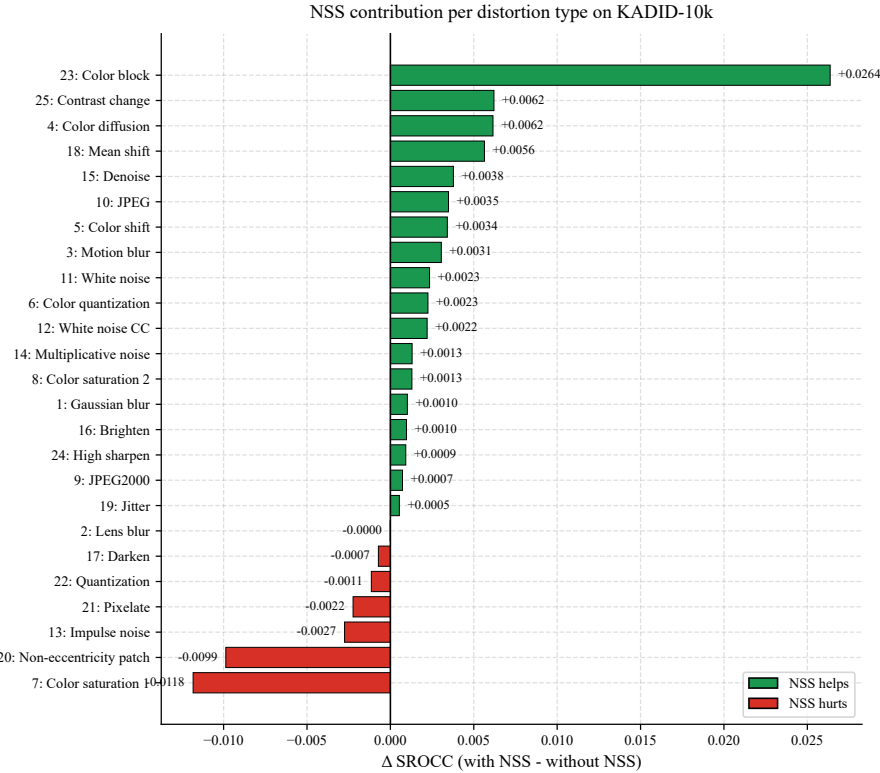


Figure 3: Per-distortion delta SROCC (NSS+SigLIP+CLIP-H minus SigLIP+CLIP-H) on KADID-10k. Green: NSS improves fusion. Red: NSS hurts fusion.

distortion types is  $\rho = 0.33$ : the model assigns higher NSS gates where NSS improves fusion and lower gates where it is harmful, The main discrepancy is Color block (type 23), which has the largest positive delta (+0.026) but a relatively low gate (0.710), attributed to the overall difficulty of this distortion type (SROCC = 0.523) preventing reliable gradient signal during training. To validate the gating input design, Fig. 5 compares three candidate inputs on both SROCC and interpretability. All three achieve nearly identical SROCC (0.970–0.971), but interpretability differs substantially: NSS-only gating yields  $\rho = 0.097$  ( $p = 0.642$ ), while SigLIP-only and CLIP-H-only achieve  $\rho = 0.33$  and  $\rho = 0.31$  respectively. SigLIP-only is selected for its highest interpretability correlation and compact 256-dimensional input.

The gate analysis demonstrates that the multiplicative gating mechanism au-

Distortion-aware gate analysis on KADID-10k  
 Multiplicative gating: learned NSS, SigLIP, and CLIP-H weights per distortion

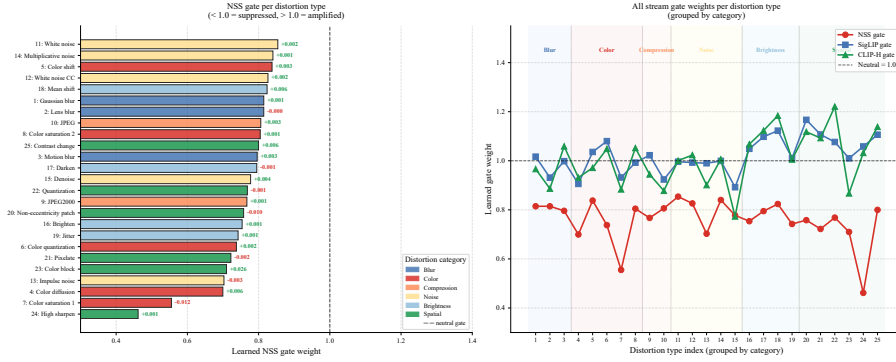


Figure 4: Gate analysis on KADID-10k. *Left*: Learned NSS gate values per distortion type sorted ascending, color-coded by category; delta SROCC from Fig. 3 annotated on each bar. *Right*: All three gate values across distortion types grouped by category. Dashed line at 1.0 is the neutral gate corresponding to static fusion.

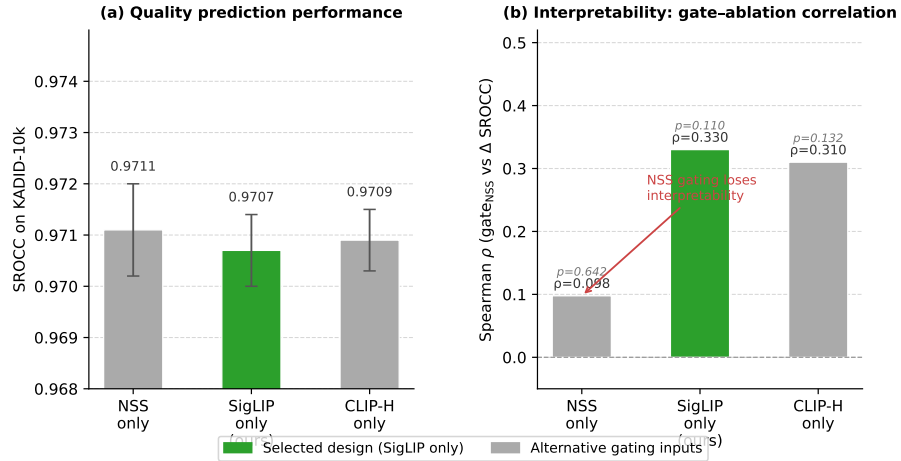


Figure 5: Gating input ablation on KADID-10k. *Left*: SROCC is nearly identical across all three options. *Right*: NSS-only gating loses interpretability ( $\rho = 0.097$ ,  $p = 0.642$ ) while SigLIP-only achieves  $\rho = 0.33$ .

tonomously discovers distortion-stream affinity patterns consistent with the manual ablation, providing independent cross-validation of the theoretical role of NSS in multi-stream BIQA fusion.

## 5. Discussion

### 5.1. Stream Complementarity

The ablation studies confirm that combining all three streams consistently outperforms any subset, with gains of 0.001–0.005 SROCC that are reproducible across all folds and several times larger than the fold-to-fold standard deviation.

The complementarity arises from fundamentally different representations. NSS features capture local pixel statistics (MSCN distributions, log-Gabor moments, color moments) that are invariant to image content and sensitive to distortions that disrupt natural statistical regularities. VLM embeddings encode content-dependent perceptual cues—naturalness, aesthetic quality, recognizability—that correlate with subjective MOS but are invisible to pixel statistics. The two paradigms are therefore largely orthogonal, and the fusion model exploits whichever signal is more reliable for a given input.

Within the VLM streams, SigLIP [20] and CLIP-H [29] contribute distinct information due to different training objectives (sigmoid vs. softmax contrastive loss) and different training data (WebLI vs. LAION-2B), consistent with recent observations that diverse VLM ensembles outperform a single scaled model on downstream tasks [24, 28].

### 5.2. Computational Efficiency

Table 6 compares the computational cost of the proposed framework against representative state-of-the-art methods. The proposed MLP regression head has only 464,897 trainable parameters, approximately  $295\times$  fewer than MANIQA [15],  $329\times$  fewer than LIQE [23], and more than  $15,000\times$  fewer than Q-Align [24]. Training the full three-stream configuration on KonIQ-10k requires approximately one hour on a standard CPU workstation, compared to tens of GPU-hours for end-to-end fine-tuned methods. At inference, the MLP head processes one image in 0.32 ms on CPU (excluding the one-time feature extraction step), making deployment practical in resource-constrained settings without dedicated hardware.

The efficiency advantage stems directly from the frozen-feature design: VLM feature extraction is a one-time offline cost performed once per dataset, after which

all training and inference operates on cached 650-dimensional vectors. This design trades a moderate performance gap on authentic-distortion benchmarks (KonIQ-10k, LIVE-itW) for orders-of-magnitude lower computational cost, making the framework particularly suitable for applications where GPU resources are unavailable or where rapid deployment across new datasets is required.

Table 6: Computational Efficiency Comparison. Inference time per image on CPU unless noted. <sup>†</sup> GPU required for inference. <sup>‡</sup> excludes one-time feature extraction.

Method	Params (M)	Train (GPU h)	Infer. (ms/img)	GPU req.
MANIQa [15]	135.7	~24	~540 <sup>†</sup>	Yes
LIQE [23]	151.3	~48	~58 <sup>†</sup>	Yes
Q-Align [24]	7,000	~96	~220 <sup>†</sup>	Yes
<b>Ours</b>	<b>0.46</b>	<b>~1<sup>‡</sup></b>	<b>0.32<sup>‡</sup></b>	<b>No</b>

### 5.3. Per-Distortion Patterns and NSS Role

NSS contributes most on distortions that directly affect global pixel statistics: Color block (+0.026), Color diffusion (+0.006), Contrast change (+0.006), Mean shift (+0.006), and Denoise (+0.004). In each case the perturbation is well-characterized by the NSS descriptor—uniform color regions disrupt intensity distributions, contrast and luminance shifts alter MSCN statistics, and denoise modifies log-Gabor sub-band energy.

NSS hurts most on Color saturation 1 (−0.012) and Non-eccentricity patch (−0.010). For color saturation, the spatial structure of the image is preserved and the chromatic change falls only on the 12 color moment dimensions of the 138-dimensional descriptor; the remaining 126 dimensions act as uninformative noise. For non-eccentricity patch, the distortion is spatially localized but the NSS aggregation is global, diluting the per-block signal.

The gate analysis (Section 4.7) validates these findings independently: the Spear-

man correlation between learned NSS gate values and per-distortion delta SROCC is  $\rho = 0.33$ , confirming that the model autonomously suppresses NSS where it is uninformative and amplifies it where it helps.

#### 5.4. LIVE-itW and Small-Dataset Generalization

The LIVE-itW results illustrate a training-set size interaction. With only  $\approx 930$  training images per fold, the full three-stream model underperforms SigLIP+CLIP-H (0.747 vs. 0.790 SROCC) and shows much higher fold variance (0.057 vs. 0.032): the NSS dimensions cause overfitting. Cross-dataset transfer from KonIQ-10k reverses this (0.811 vs. 0.807), and the full pretrain+finetune+ensemble protocol widens the gap to 0.853 vs. 0.849. The NSS stream therefore requires sufficient training data to learn appropriate weighting; on large datasets it contributes genuine complementary signal.

#### 5.5. Limitations

Several limitations point to future work. First, the frozen-feature design imposes a performance ceiling: end-to-end fine-tuned methods such as Q-Align [24] achieve higher SROCC on KonIQ-10k and LIVE-itW by adapting the backbone to the IQA task. Second, the per-distortion analysis is limited to KADID-10k because authentic-distortion datasets do not provide distortion-type labels; extending the analysis to TID2013 or PIPAL would broaden the findings. Third, the block-based global NSS aggregation is insensitive to spatially localized distortions; region-specific or attention-based NSS variants could address the weakness on Color block and Non-eccentricity patch. Finally, the framework has not been tested on AI-generated content (AIGC); datasets such as AGIQA-3k [1] and AIGCIQA2023 [2] offer a natural extension target.

## 6. Conclusion

We proposed a distortion-aware three-stream fusion framework for blind image quality assessment combining a 138-dimensional NSS descriptor with SigLIP and CLIP-H vision-language embeddings through a multiplicative gating mechanism and a hybrid MSE+PLCC+ranking loss. The framework requires no end-to-end VLM

fine-tuning and trains only  $\approx 466,000$  parameters on CPU, achieving state-of-the-art SROCC of 0.9715 on KADID-10k, surpassing MANIQA, LIQE, and Q-Align on the most challenging synthetic-distortion benchmark.

A per-distortion analysis reveals that NSS contributes most on distortions that directly affect pixel statistics (color block, contrast change, noise) and least on perceptual or spatially localized distortions (color saturation, non-eccentricity patch). The learned gate values independently confirm this pattern with  $\rho = 0.33$ , and a gating input ablation further shows that SigLIP-only gating maximizes interpretability while NSS-only gating collapses to  $\rho = 0.097$ , validating the design choice.

These results support a broader conclusion: classical NSS features retain practical value alongside billion-parameter VLMs when integrated through an appropriately designed fusion architecture. Future directions include end-to-end backbone fine-tuning, region-specific NSS descriptors for spatially localized distortions, and extension to AI-generated content quality assessment [1, 2].

### **Author Contributions**

Bishr Omer Abdelrahman Adam: Conceptualization, Methodology, Software, Investigation, Formal analysis, Writing original draft. Xu Li: Supervision, Funding acquisition, Writing review & editing. All authors have read and approved the final version of the manuscript.

### **Acknowledgements**

This work is supported by the Key Research and Development Program of Shaanxi Province (No. 2025CY-YBXM-079). The authors thank the Kaggle platform for providing free GPU access used for one-time VLM feature extraction. The authors also thank the creators of KonIQ-10k, KADID-10k, and LIVE-itW for making their datasets publicly available to the research community.

### **Declaration of Competing Interest**

The authors declare that they have no known competing financial interests or personal relationships that could have appeared to influence the work reported in this paper.

### **Data Availability**

The three datasets used in this study are publicly available. KonIQ-10k is available at: <https://database.mmmsp-kn.de/koniq-10k-database.html>. KADID-10k is available at <http://database.mmmsp-kn.de/kadid-10k-database.html>. LIVE Challenge in-the-Wild is available at <https://live.ece.utexas.edu/research/ChallengeDB/index.html>. The source code, extracted feature files, and trained model weights are publicly available at <https://github.com/bishr-omer/multimodal-biqa>.

### **Declaration of Generative AI and AI-Assisted Technologies in the Manuscript Preparation Process**

During the preparation of this work the authors used Claude (Anthropic) in order to assist with code debugging, LaTeX formatting and language editing. After using this tool/service, the authors reviewed and edited the content as needed and take full responsibility for the content of the published article.

### **References**

- [1] J. Li, T. Wu, J. Wang, P. Zhou, Z. Yang, and Q. Yan, "AGIQA-3k: An open database for AI-generated image quality assessment," *IEEE Trans. Circuits Syst. Video Technol.*, vol. 34, no. 8, pp. 6833–6846, 2024.
- [2] J. Wang, H. Duan, J. Liu, S. Chen, X. Min, and G. Zhai, "AIGCIQA2023: A large-scale image quality assessment database for AI generated images: From the perspectives of quality, authenticity and correspondence," in *Proc. CAAI Int. Conf. Artif. Intell.*, 2023, pp. 46–57.

- [3] A. Mittal, A. K. Moorthy, and A. C. Bovik, “No-reference image quality assessment in the spatial domain,” *IEEE Trans. Image Process.*, vol. 21, no. 12, pp. 4695–4708, 2012.
- [4] A. Mittal, R. Soundararajan, and A. C. Bovik, “Making a ‘completely blind’ image quality analyzer,” *IEEE Signal Process. Lett.*, vol. 20, no. 3, pp. 209–212, 2013.
- [5] L. Zhang, L. Zhang, and A. C. Bovik, “A feature-enriched completely blind image quality evaluator,” *IEEE Trans. Image Process.*, vol. 24, no. 8, pp. 2579–2591, 2015.
- [6] A. K. Moorthy and A. C. Bovik, “Blind image quality assessment: From natural scene statistics to perceptual quality,” *IEEE Trans. Image Process.*, vol. 20, no. 12, pp. 3350–3364, 2011.
- [7] X. Hao, X. Li, J. Wu, B. Wei, Y. Song, and B. Li, “A no-reference quality assessment method for hyperspectral sharpened images via Benford’s law,” *Remote Sens.*, vol. 16, no. 8, p. 1167, 2024.
- [8] J. Wu, X. Li, B. Wei and L. Li, “A no-reference spectral quality assessment method for multispectral pansharpening,” in *Proc. IEEE Int. Geosci. Remote Sens. Symp. (IGARSS)*, Pasadena, CA, USA, Jul. 2023.
- [9] W. Zhang, K. Ma, J. Yan, D. Deng, and Z. Wang, “Blind image quality assessment using a deep bilinear convolutional neural network,” *IEEE Trans. Circuits Syst. Video Technol.*, vol. 30, no. 1, pp. 36–47, 2020.
- [10] S. Su, Q. Yan, Y. Zhu, C. Zhang, X. Ge, J. Sun, and Y. Zhang, “Blindly assess image quality in the wild guided by a self-adaptive hyper network,” in *Proc. IEEE/CVF CVPR*, 2020, pp. 3667–3676.
- [11] I. Loshchilov and F. Hutter, “SGDR: Stochastic gradient descent with warm restarts,” in *Proc. ICLR*, 2017.

- [12] W. Zhang, K. Ma, G. Zhai, and X. Yang, “Uncertainty-aware blind image quality assessment in the laboratory and in the wild,” *IEEE Trans. Image Process.*, vol. 30, pp. 3474–3486, 2021.
- [13] S. A. Golestaneh, S. Dadsetan, and K. M. Kitani, “No-reference image quality assessment via transformers, relative ranking, and self-consistency,” in *Proc. IEEE/CVF WACV, 2022*, pp. 3989–3999.
- [14] J. Ke, Q. Wang, Y. Wang, P. Milanfar, and F. Yang, “MUSIQ: Multi-scale image quality transformer,” in *Proc. IEEE/CVF ICCV, 2021*, pp. 5148–5157.
- [15] S. Yang, T. Wu, S. Shi, S. Lao, Y. Gong, M. Cao, J. Wang, and Y. Yang, “MANIQA: Multi-dimension attention network for no-reference image quality assessment,” in *Proc. IEEE/CVF CVPRW, 2022*, pp. 1191–1200.
- [16] M. U. Rehman, I. F. Nizami, F. Ullah, and I. Hussain, “IQA vision transformed: A survey of transformer architectures in perceptual image quality assessment,” *IEEE Access*, vol. 12, pp. 183369–183393, 2024.
- [17] L. Agnolucci, L. Galteri, M. Bertini, and A. Del Bimbo, “ARNIQA: Learning distortion manifold for image quality assessment,” in *Proc. IEEE/CVF WACV, 2024*, pp. 3344–3353.
- [18] K. Xu, L. Liao, J. Xiao, C. Chen, H. Wu, Q. Yan, and W. Lin, “Boosting image quality assessment through efficient transformer adaptation with local feature enhancement,” in *Proc. IEEE/CVF CVPR, 2024*, pp. 2662–2672.
- [19] A. Radford, J. W. Kim, C. Hallacy, A. Ramesh, G. Goh, S. Agarwal, G. Sastry, A. Askell, P. Mishkin, J. Clark, G. Krueger, and I. Sutskever, “Learning transferable visual models from natural language supervision,” in *Proc. ICML, 2021*, pp. 8748–8763.
- [20] X. Zhai, B. Mustafa, A. Kolesnikov, and L. Beyer, “Sigmoid loss for language image pre-training,” in *Proc. IEEE/CVF ICCV, 2023*, pp. 11975–11986.

- [21] J. Wang, K. C. K. Chan, and C. C. Loy, “Exploring CLIP for assessing the look and feel of images,” in *Proc. AAAI*, vol. 37, no. 2, 2023, pp. 2555–2563.
- [22] S. Zhao, H. Zhou, X. Li, Y. Fang, and H. Zhu, “Quality-aware pre-trained models for blind image quality assessment,” in *Proc. IEEE/CVF CVPR*, 2023, pp. 22–31.
- [23] W. Zhang, G. Zhai, Y. Wei, X. Yang, and K. Ma, “Blind image quality assessment via vision-language correspondence: A multitask learning perspective,” in *Proc. IEEE/CVF CVPR*, 2023, pp. 14071–14081.
- [24] H. Wu, Z. Zhang, W. Zhang, C. Chen, L. Liao, C. Li, Y. Gao, A. Wang, E. Zhang, W. Sun, Q. Yan, X. Min, G. Zhai, and W. Lin, “Q-Align: Teaching LMMs for visual scoring via discrete text-defined levels,” in *Proc. ICML*, 2024, pp. 54015–54029.
- [25] Z. You, X. Cai, J. Gu, T. Xue, and C. Dong, “Teaching large language models to regress accurate image quality scores using score distribution,” in *Proc. IEEE/CVF CVPR*, 2025, pp. 14483–14494.
- [26] X. Chen, H. Zhang, R. Lu, L. Gu, X. Chu, J. Qiao, and C. Dong, “TOPIQ: A top-down perspective for image quality assessment,” *IEEE Trans. Image Process.*, vol. 33, pp. 2940–2955, 2024.
- [27] Z. Ying, H. Niu, P. Gupta, D. Mahajan, D. Ghadiyaram, and A. C. Bovik, “From patches to pictures (PaQ-2-PiQ): Mapping the perceptual space of picture quality,” in *Proc. IEEE/CVF CVPR*, 2020, pp. 3575–3585.
- [28] H. Wu, Z. Zhang, E. Zhang, C. Chen, L. Liao, A. Wang, C. Li, W. Sun, Q. Yan, G. Zhai, and W. Lin, “Q-Bench: A benchmark for general-purpose foundation models on low-level vision,” in *Proc. ICLR*, 2024.
- [29] G. Ilharco, M. Wortsman, R. Wightman, C. Gordon, N. Carlini, R. Taori, A. Dave, V. Shankar, H. Namkoong, J. Miller, H. Hajishirzi, A. Farhadi, and L. Schmidt, “OpenCLIP,” Software, 2021. [Online]. Available: [https://github.com/mlfoundations/open\\_clip](https://github.com/mlfoundations/open_clip)

- [30] V. Hosu, H. Lin, T. Sziranyi, and D. Saupe, “KonIQ-10k: An ecologically valid database for deep learning of blind image quality assessment,” *IEEE Trans. Image Process.*, vol. 29, pp. 4041–4056, 2020.
- [31] H. Lin, V. Hosu, and D. Saupe, “KADID-10k: A large-scale artificially distorted IQA database,” in *Proc. QoMEX*, 2019, pp. 1–3.
- [32] D. Ghadiyaram and A. C. Bovik, “Massive online crowdsourced study of subjective and objective picture quality,” *IEEE Trans. Image Process.*, vol. 25, no. 1, pp. 372–387, 2016.
- [33] B. O. Adam, X. Li, J. Wu, and X. Hao, “A no-reference multivariate Gaussian-based spectral distortion index for pansharpened images,” *Sensors*, vol. 26, 2026.
- [34] I. Loshchilov and F. Hutter, “Decoupled weight decay regularization,” in *Proc. ICLR*, 2019.
- [35] Y. Fang, H. Zhu, Y. Zeng, K. Ma, and Z. Wang, “Perceptual quality assessment of smartphone photography,” in *Proc. IEEE/CVF CVPR*, 2020, pp. 3677–3686.